

Heterologous expression, purification and structural features of native *Dictyostelium discoideum* dye-decolorizing peroxidase bound to a natively incorporated heme

Özlem Kalkan^{1,2}, Sravya Kantamneni¹, Lea Brings¹, Huijong Han¹, Adrian P. Mancuso^{1,3,4}, and Faisal H.M. Koua^{1,2*}

¹European XFEL GmbH, Holzkoppel 4, D-22869 Schenefeld, Schleswig-Holstein, Germany.

²Department of Molecular Biology and Genetics, Faculty of Science, Istanbul University, 34134 Istanbul, Turkey.

³La Trobe Institute for Molecular Science, La Trobe University, Melbourne, Victoria 3086, Australia.

⁴Diamond Light Source Ltd., Harwell Science and Innovation Campus, Didcot, OX11 0DE, United Kingdom.

* Correspondence:

Corresponding Author

faisal.koua@xfel.eu

Keywords: Biocatalysis, Dye-decolorizing peroxidases, Heme incorporation, Lignin degradation, Polycyclic dyes, structure enzymology, redox catalysis.

Abstract

The *Dictyostelium discoideum* dye-decolorizing peroxidase (*DdDyP*) is a newly discovered peroxidase, which belongs to a unique class of heme peroxidase family that lacks homology to the known members of plant peroxidase superfamily. *DdDyP* catalyzes the H₂O₂-dependent oxidation of a wide-spectrum of substrates ranging from polycyclic dyes to lignin biomass, holding promise for potential industrial and biotechnological applications. To study the molecular mechanism of *DdDyP*, highly pure and functional protein with a natively incorporated heme is required, however, obtaining a functional DyP-type peroxidase with a natively bound heme is challenging and often requires addition of expensive biosynthesis precursors. Alternatively, a heme *in vitro* reconstitution approach followed by a chromatographic purification step to remove the excess heme is often used. Here, we show that expressing the *DdDyP* peroxidase in 2×YT enriched medium at low temperature (20 °C), without adding heme supplement or biosynthetic precursors, allows for a correct native incorporation of heme into the apo-protein, giving rise to a stable protein with a strong Soret peak at 402 nm. Further, we crystallized and determined the native structure of *DdDyP* at a resolution of 1.95 Å, which verifies the correct heme binding and its geometry. The structural analysis also reveals a binding of two water molecules at the distal site of heme plane bridging the catalytic residues (Arg239 and Asp149) of the GXXDG motif to the heme-Fe(III) via hydrogen bonds. Our results provide new insights into the geometry of native *DdDyP* active site and its implication on DyP catalysis.

1 Introduction

The *Dictyostelium discoideum* dye-decolorizing peroxidase (*DdDyP*) is a newly discovered heme peroxidase (Sugano et al., 2007). *DdDyP* belongs to a new class of DyP-type peroxidases (EC 1.11.1.19), which is different from any other known peroxidases (Kim et al., 1999; Sugano et al., 1999;

Sugano et al., 2007; Shrestha et al., 2016). This unique peroxidase family has been shown to perform both H₂O₂-dependent oxidation and hydrolytic functions against a wide-spectrum of substrates, ranging from polycyclic dyes, phenolic compounds, sulfides, carotenoids and interestingly lignin biomass, making it a potential candidate for industrial and biotechnological applications including its possible application as bioenergy catalysts as well as biosurfactants in the biodegradation and biotransformation of emerging environmental contaminants (Gan et al., 2022; Rai et al., 2021; Salvachua et al., 2013; Sugano et al., 2021; Xu et al., 2021). This broad substrate specificity is attributed to their unique sequence identity and structural properties (Kim et al., 1999; Yoshida and Sugano, 2023). *DdDyP*, as other peroxidases, has been found to function in a wide range of pH milieu displaying higher activity at acidic pH with optimal turnover at pH 4.0 and temperatures ranging from 20 to 40 °C (Rai et al., 2021; Xu et al., 2021; Colpa et al., 2014). It shows optimal activity at pH 3.0 against the known DyP-type peroxidase substrate—the anthraquinone-based dye RB4 (Rai et al., 2021).

DyP-type peroxidases share a typical catalytic mechanism with other peroxidases, in which they depend on the H₂O₂ in their oxidative catalytic function as illustrated in scheme 1 (Scocozza et al., 2021; Sugano and Yoshida, 2021). The resting state of the enzyme proceeds into compound I intermediate state upon interaction of the heme-Fe(III) with hydrogen peroxide (H₂O₂), an oxidizing substrate, forming an oxoferryl porphyrin π -cationic radical complex [Fe(IV)=O Por[•]]⁺—a porphyrinoid based radical (Colpa et al., 2014; Scocozza et al., 2021). The release of an electron from compound I leads to the formation of compound II [Fe(IV)=O]⁺ intermediate upon reaction with a reducing substrate giving rise to a radical product, in turn compound II relaxes into the resting state when it reacts with more substrates (Chen et al., 2015; Shrestha et al., 2016; Sugano and Yoshida, 2021). The radical product can then be transformed into various sub-products through a non-enzymatic radical coupling. The redox potential of the DyP-type peroxidases, ranging from -50 mV to +250 mV, and that of the substrate determines the feasibility of enzyme catalysis. Generally, a typical DyP-peroxidase catalysis involves several redox couplings, namely Fe³⁺/Fe²⁺, compound I/Fe³⁺, compound II/compound I and compound II/Fe³⁺ (Shrestha et al., 2016). DyP peroxidases also mediate the hydrolysis of substrates such as anthraquinone dyes, implying that the DyP-type peroxidases are bifunctional enzymes (Colpa et al., 2014). However, the exact mechanism for DyP-type peroxidases and how they perform oxidation and hydrolysis for such a wide range of substrates of different chemical properties remain unclear (Xu et al., 2021; Sugano and Yoshida, 2021).

Despite the importance of the DyP-type peroxidases as mentioned above, their heterologous expression in *Escherichia coli* (*E. coli*) and other expression systems remain challenging. It hampers, for instance, on the large-scale mechanistic investigation owing to the difficulties associated with the biosynthesis and availability of heme *b*, thereby limiting its native incorporation into the apo-proteins (Fiege et al., 2018; Park and Kim, 2021). It was previously shown that *in vitro* reconstitution is needed for obtaining functional *DdDyP* with the correct heme stoichiometry (Rai et al., 2021). This is an inherently time-consuming process and may result in excess heme and unspecific binding or altering the protein function, making it limited to robust proteins only (Vogel et al., 1999; Denninger et al., 2000; Lemon et al., 2021). Alternatively, heme and iron supplements or heme biosynthetic precursors such as δ -aminolevulinic acid (δ -ALA) can be used during expression, however this is a highly expensive approach as large amounts of such supplements are needed (Fiege et al., 2018).

Here, we report on the use of *E. coli* OverExpress C43(DE3) strain for the expression and production of the *DdDyP* peroxidase without heme supplement nor its precursor δ -ALA. Furthermore, using X-ray structural analyses, we describe the first crystal structure of native *DdDyP* peroxidase bound to a natively incorporated heme and demonstrate that the geometry of the heme binding pocket resembles

in much detail that of a previously reported cyanide native *DdDyP* structure, which was prepared following *in vitro* heme reconstitution approach.

2 Methods

2.1 Overexpression and purification of *DdDyP* with natively incorporated heme

The gene sequence encoding dye-decolorizing peroxidase from the slime mold *D. discoideum* AX4 (GenBank: EAL70759.1) was codon optimized for *Escherichia coli*, synthesized and subcloned into the *Bam*HI/*Xho*I cloning site in a pGEX-6P1 vector harboring a Human Rhinovirus 3C excision site and a glutathione transferase (GST) tag at the N-terminal region (BioCat GmbH, Germany). The pGEX-6P1-*DdDyP* construct was transformed into an OverExpress *E. coli* C43(DE3), a chemically competent strain (Sigma-Aldrich, Germany). For purification, a single colony from a freshly streaked plate was inoculated into a Luria-Bertani (LB) or 2×YT enriched media containing 100 µg ml⁻¹ final concentration of ampicillin and incubated at 37 °C for overnight (15-16 h). A starter culture was used to inoculate 6× 1L of LB or 2×YT containing 100 µg ml⁻¹ ampicillin and incubated at 37 °C or lower temperatures until the optical density (OD₆₀₀) reaches 1.0-1.25 before inducing the expression of *DdDyP* with 1.0 mM of isopropyl β-D-1-thiogalactopyranoside. The culture was then incubated for additional 7 h or 20 h for expression at 37 and 20 °C, respectively. The cells were harvested by centrifugation with 13,881 ×g for 30 min on an F9-6-×1000 LEX rotor (Thermo Fischer Scientific, Germany) at 4 °C and pellets were stored at -80 °C until used.

For protein purification, frozen cells were thawed using warm tap water (~40 °C) and diluted with 3-5× of lysis buffer containing 0.05 M Tris-HCl, pH 8.0 and 0.15 M NaCl supplemented with 1.0 mM final concentration of phenylmethylsulfonyl fluoride protease inhibitor or a tablet of EDTA-free protease inhibitor cocktail (Sigma-Aldrich, Germany). The cells were lysed with 35 cycles of sonication at 4 °C on ice using 50% amplitude and 25 sec sonication pulse with 1.5 min interval. Lysate was clarified with centrifugation at 52,400 ×g at 4 °C for 45 min and the supernatant was filtered with a 0.45 µm syringe filter and mixed with 5-10 ml glutathione sepharose high-performance resin pre-equilibrated with lysis buffer, followed by incubation at 4 °C with gentle rotation for 3 h. The mixture was loaded into an empty gravity column and the GST-tagged *DdDyP* was eluted with 5× column volume of an elution buffer containing 0.05 M Tris-HCl, pH 8.0, 0.15 M NaCl and 15-20 mM L-Glutathione (reduced form). The GST tag was then removed using HRV 3C protease with 1:20 enzyme to protein ratio at 4 °C for overnight followed by passing the mixture through a glutathione sepharose column pre-equilibrated with lysis buffer. Purified protein was characterized with SDS-PAGE and UV-visible spectrophotometry. For crystallization the protein was further purified with gel-filtration using Superdex 75 10/300 Increase column (Cytiva, Sweden). Purified protein was concentrated to 20-30 mg ml⁻¹ in lysis buffer and stored at -80 °C until further use. Overexpression, purification and crystallization were carried out the XBI BioLab of the European XFEL facility (Han et al., 2021).

2.2 Heme reconstitution

A control heme reconstitution experiment was conducted as described previously (Chen et al., 2015). In brief, purified apo-*DdDyP* from LB expression was mixed with hemin chloride with ~1:2 molar ratio in a buffer containing 50 mM Tris-HCl, pH 7.0 and 150 mM NaCl, followed by incubation on ice for 30 min. The heme reconstituted holo-*DdDyP* protein was then passed through a PD-10 desalting column (Cytiva, Sweden) to remove the excess hemin chloride.

2.3 UV-visible spectrophotometry

All spectra were recorded on a Shimadzu UV-2700 PC spectrophotometer (Shimadzu Co., Japan) using a cuvette with 1.0 cm pathlength in a range of 200-700 nm at room temperature (20 ± 2.0 °C). For measurements purified *DdDyP* was diluted with lysis buffer to a concentration of 0.4 mg ml⁻¹ and the lysis buffer was used as a reference. All spectra were processed using the Origin software 2022b (OriginLab Co., USA).

2.4 Crystallization screening and crystal optimization of *DdDyP*

Crystallization screening was performed using a NT8 Formulatrix robot (Formulatrix, USA). Hit was obtained from the C12 condition (20% PEG 6000, 0.1 M HEPES, pH 7.0, 0.01 M ZnCl₂) of the PACT++ crystallization screen (Jena Bioscience, Germany) with 10 mg ml⁻¹ of purified *DdDyP*. This condition was further optimized to 15% PEG 6000, 0.1 M HEPES-NaOH, pH 7.0, and 0.01 M ZnCl₂ crystallized with 15 mg ml⁻¹ final concentration of purified *DdDyP*, which gave rise to a maximum crystal size of $200 \times 100 \times 25$ μm at 20 °C in 4-6 weeks. Crystals were harvested directly from the drops using nylon loops and flash-cooled in liquid nitrogen.

2.5 X-ray diffraction data collection, processing and structure determination

X-ray diffraction datasets were collected at the P11/PETRA III beamline at DESY (Hamburg, Germany) using a flat focus with 20×20 μm² (v × h) beam area at the sample position, 12.0 keV photon energy, and a photon flux of $\sim 2 \times 10^{10}$ photon sec⁻¹ and an exposure time of 100 ms for a total wedge of 360° with 0.1° oscillation recording step on EIGER 16M detector (Burkhardt et al., 2016). Data collection were performed at cryogenic temperature, 100K. Diffraction datasets were processed using the program XDS, and scaled with XSCALE in the XDS graphic user interface (Kabsch, 2010). The initial phase was obtained by molecular replacement using the *DdDyP* peroxidase active structure (PDB ID: 7ODZ) as a reference model with the program Phaser in the phenix software (Afonine et al., 2012). The model was then refined in phenix and manually corrected in coot (Emsley et al., 2010). Radiation dose was estimated using the program RADDOSE-3D as described previously using the abovementioned parameters (Bury et al., 2018). For channel and cavity calculations *MOLEontile* tool (<https://mole.uplo.cz/method>) was used with the coordinate obtained from the final cycle of refinement (PDB ID: 8OHY) as a template (Sehnal et al., 2013). The interfaces of heme *b* and the oligomeric states analysis of *DdDyP* were calculated using PISA (Protein Interfaces, Surfaces, and Assemblies) server (Krissinel and Henrick, 2007).

3 Results and Discussion

3.1 Heterologous expression and characterization of *DdDyP*

For heterologous expression, a *DdDyP* peroxidase gene was cloned into a pGEX-6P1 vector which has an HVR 3C excision site and a GST-tag in its N-terminal region as reported previously (Rai et al., 2021), however, we used the OverExpress *E. coli* C43(DE3) strain instead of BL21 for overexpression screening. *DdDyP* was expressed at high and low temperature (37 and 20 °C) in LB and 2×YT medium with different yields, ranging from 2.1 and 14.1 mg of protein in average per 25 g of cells, respectively (Table 1). Figure 1A-B shows the SDS-PAGE analyses of the typical expression and purification of *DdDyP* in *E. coli* C43(DE3) strain. Protein expressed at 37 °C, however, has transparent to pale brownish colour, whereas those of 20 °C exhibited a darker brownish colour (Figure 1C). The proteins purified from high and low temperature have a reasonable purity with less aggregation (Figure 1) with ~35 kDa molecular weight as confirmed by the SDS-PAGE analysis. However, no crystallization hit was obtained from these conditions despite several attempts with various crystallization screens (Table

1). Since that our purified *DdDyP* has sufficient purity for crystallization, yet we did not successfully crystallize it, we concluded that the instability of the protein during expression at 37 °C may be the cause for the unsuccessful crystallization. This is likely due to the improper protein folding, and thus lowering the temperature of the expression may be one method for achieving a stable and correctly folded protein (Francis and Page, 2010; Huang et al., 2021). Indeed, when we expressed *DdDyP* at 20 °C, it gave rise to a darker brownish protein (Figure 1C), a typical heme peroxidase colour of a native protein, especially when expressed in a 2×YT enriched medium, which is richer than LB. Intriguingly, *DdDyP* expressed in 2×YT at lower temperature was the only condition that resulted in a successful crystallization yielding dark brownish crystals, an indication that heme *b* is preserved during purification and crystallization (Figure 1D). The 2×YT also yielded several times higher amount of protein than that obtained in LB (Table 1).

To examine the quality of the electronic absorbance of purified *DdDyP* we used a UV-visible spectrophotometer. Figure 2 shows the spectral analysis of the purified *DdDyP* protein from different conditions. *DdDyP* shows weak absorbance Soret peak at $\lambda = 405$ nm and a Reinheitszahl (R_Z) (A_{soret}/A_{280}) value of ~0.27 when expressed in LB at 37 °C (Table 1). This R_Z value is about 2 times higher than that obtained previously on peroxidases that were expressed using BL21(DE3) strain (Rai et al., 2014; Fiege et al., 2018). As shown in Table 1, we observed that the R_Z value increases ×2–3 times to reach ~0.93 with $\lambda = 402$ nm of the Soret peak when expressing *DdDyP* in enriched 2×YT medium at low temperature (20 °C). This value is comparable to our heme reconstitution reference (Figure 2E) and significantly higher (about 7 times) than those previously reported, when DyP-peroxidases were expressed without adding heme supplements or δ -ALA during expression (Fiege et al., 2018; Krainer et al., 2015). Heme biosynthesis in *E. coli* relies on an L-glutamate amino acid and other proteinoid biochemicals which are abundant in both tryptone and yeast extracts—major components in 2×YT and LB medium (Layer et al., 2010; Krainer et al., 2015). The 2×YT medium has a double amount of tryptone and yeast extracts comparing to LB medium. This might explain the higher level of heme biosynthesis, and thus the native incorporation into *DdDyP*, in 2×YT than that in LB (Table 1). The heme reconstituted *DdDyP* from LB expression shows a Soret absorbance at 406 nm and an electron transfer (ET) (*Q*-band) at $\lambda = 497$ nm plus two additional ET bands at 536 nm and 576 nm as well as a charge transfer (CT) component at 636 nm, preserving some bacterial peroxidase features (Chen and Li, 2016). This region differs significantly from that previously reported in *DdDyP*, which showed an ET and CT band at 506 nm and 636 nm, respectively (Rai et al., 2021). We also observed that the *DdDyP* with a natively incorporated heme has a broad ET peak with $\lambda_{\text{max}} = 508$ nm, which is slightly red shifted with $\Delta\lambda = 9$ nm and $\Delta\lambda = 2$ nm, comparing to that of the ET bands of the reference (Figure 2) and a previous work, respectively (Rai et al., 2021). The *Q*-band region also reveals a unique shoulder at the ET band with 567 nm absorbance (Figure 2C).

3.2 Native structure of *DdDyP* peroxidase bound to a water molecule

Several *DdDyP* structures have been resolved so far including a single native structure that is in complex with cyanide (PDB: 7O9L) (Rai et al., 2021), however there is no available structure that describes the native resting state. Here, to get insight into the heme binding pocket in its native form, we crystallized the native *DdDyP* peroxidase bound to a natively incorporated heme and compared it with that resolved in complex with cyanide. A single crystal with a size of $150 \times 80 \times 30 \mu\text{m}^3$ size was used for diffraction data collection (Figure 1D). The crystal data collection and refinement statistics are shown in Table 2. Native *DdDyP* peroxidase is crystallized in a tetragonal space group $P4_1 2_1 2$ similar to previously reported structures (Rai et al., 2014), with exception that the X-ray data of the current crystal condition can be equally processed and resolved in an additional space group ($P4_3 2_1 2$) (Table 2). Moreover, the crystal unit cell exhibited significantly shorter axes, giving rise to about 35%

smaller cell volume with 52.8% solvent content and $2.62 \text{ \AA}^3 \text{ Da}^{-1}$ of Matthew's coefficient (V_m), indicating the presence of a single molecule per asymmetric unit. The solvent content is decreased by ~20% comparing to that previously reported (Rai et al., 2021). This is more likely due to a relatively high concentration of the dehydrating precipitant (~30% PEG 6000), as previously reported in other systems (Umena et al., 2011; Koua et al., 2013). Such high PEG concentration causes a shrinking in the protein crystals by dehydration which shorten the axes and leads to a tightly packed unit cell (Figure S1). The average radiation dose on a single crystal was estimated with RADDOSE-3D (Bury et al., 2018) to be ~0.58 MGy ($\text{Gy} = \text{J} \cdot \text{kg}^{-1}$) (Table 2) which lies well below the 20 MGy dose limit suggested by Henderson (Henderson, 1990) or the 30 MGy suggested by Owen and Garman (Owen et al., 2006), indicating that the structure is less affected by radiation damage.

The overall architecture of *DdDyP* is similar to that of the typical DyP-type peroxidase superfamily (Sugano et al., 2007; Chen et al., 2015; Rai et al., 2021). *DdDyP* contains a duplicated ferredoxin-like fold domain arranged as a β -barrel at the N- and C-terminals of the protein (Figure 3). It contains 12 β -sheets and 13 α -helices formed by 185 residues of the full chain (306 residues), and the remaining 121 residues involved in the formation of loop structures that link these secondary structures. Similar to all other known DyP-type peroxidases, *DdDyP* contains α -helices with a unique β -sheet structure at the distal region of the heme plane (Strittmatter et al., 2013; Sugano et al., 2007). We determined the root mean square deviation (r.m.s.d.) between the C α (1-306 residues) of the present structure with that resolved in complex with cyanide (PDB ID: 7O9L) to be 0.18 \AA , indicating the striking similarity between the two structures. Our PISA analysis predicted a stable dimer of *DdDyP* in solution with 33 residues contributing to the dimer interface, similar to previously reported *DdDyP* structures (Rai et al., 2021). These interfacial residues are distributed along the dimer interface from the N- to the C-terminal region. The dimeric structure reveals a solvent accessible area of 24290 \AA^2 and buried surface areas (BSA) of 5330 \AA^2 , corresponding to about 22% of the total surface area of the protein. On the other hand, the BSA of the monomeric structure is 1341 \AA^2 , corresponding to 9.6% of the total surface area of monomeric *DdDyP*. It should be noted that our PISA analysis favoured a tetramer oligomeric state for the native cyanide *DdDyP* (PDB ID: 7O9L) structure, displaying higher binding energy than that of the dimeric state. This indicates that *DdDyP* protein may exist physiologically in various oligomeric states. Indeed, several DyP-type peroxidases have been reported to exist in different functional oligomeric states ranging from monomeric to tetrameric state (Yoshida et al., 2016; Pfanzagl et al., 2020; Liu et al., 2011; Zubieta et al., 2007). The catalytic arginine residue, Arg239 in *DdDyP*, has been suggested to play a role in the protein oligomerization owing to its location and hydrogen bonding network with surface residues (Chen et al., 2015; Singh et al., 2012). In *DdDyP*, Arg239 is buried in the hydrophobic cavity of the heme binding pocket, excluding its contribution in *DdDyP* oligomerization. Moreover, our molecular replacement attempts aiming for a dimeric solution was not successful, thus we can reasonably conclude that our purified *DdDyP* favours a monomeric state in crystal. It has been previously reported, based on sedimentation velocity analysis with analytical ultracentrifugation, that dimeric *DdDyP* predominates in solution, which yielded a dimeric crystal structure (Rai et al., 2021). The crystal packing behaviour of the present structure (PDB ID: 8OHY) is significantly different from that described previously (Rai et al., 2021), likely due to a significantly low unit cell volume which exerts tight interactions between molecules in the unit cell (Figure S1). Note that the molecular contact within the unit cell is contributed by similar regions in both forms that is primarily the loop and β -sheet of the ferredoxin-fold like domain II at the C-terminal region (Figure S1).

3.3 Geometry of a natively incorporated heme, its binding pocket and the implication in catalysis

Heme *b* in the DyP-type peroxidases, a protoheme IX, is either penta- or hexacoordinated (Sugano et al., 2007; Singh et al., 2012; Rodrigues et al., 2021). The native structure of *DdDyP* accommodates heme *b* in a hydrophobic binding pocket flanked by the unique β -sheet at the distal side of the heme plane, the α -helices of the ferredoxin-like fold domain II (Figure 4) and a distinct long loop at its proximal side similar to previously reported DyP structures (Sugano et al., 2007; Zubieta et al., 2007; Liu et al., 2011). Our structural analysis shows that the native *DdDyP* heme is hexacoordinated, of which the pyrrole rings of porphyrin contributed to tetradentate chelation via their nitrogen atoms and via the conserved His222 at the proximal side with a distance of 2.11 Å. The sixth coordination is provided by a water molecule (wat-184) with a distance of 2.79 Å, which is shorter by ~0.1 Å than that of the reported Fe(III)—CN distance, indicating a stronger coordination to Fe(III) (Figure 4C). This distance is typical for Fe(III) of the resting state, implying that the model is unaltered by radiation damage (Chen et al., 2015). Wat-184 forms a strong hydrogen bond (~2.2 Å) with wat-182 and a weaker hydrogen bond with the catalytic residue Arg239 (Figure 4C). Intriguingly, the environment of our native *DdDyP* heme binding pocket is similar to that of the bacterial DypB peroxidases (Chen et al., 2015). We observed that wat-184 has slightly higher *B*-factor than wat-182, which may indicate its mobility and higher reactivity. On the other hand, wat-182 interacts via strong hydrogen bonds with the second catalytic residue Asp149 as well as Ser241, suggesting that these residues may act as proton acceptors to the H₂O₂ during the formation of compound I oxyferryl thereby contributing to its stabilization along with Arg239 (Figure 4C) as revealed in other A-type DyP peroxidases (Pfanagl et al., 2018). The binding pocket is extensively occupied with water molecules which are in hydrogen bonding interaction with nearby residues that contribute to the heme stability (Figure 4C). Note that two of the water molecules (wat-150 and wat-159), which are in hydrogen bonding interaction with Asp149 and Arg137 near the heme access channel, substituted the 1,2-ethanediol molecule in the cyanide native structure that shifted Asp149 carboxylate group towards the cyanide, giving rise to increased *B*-factor of Asp149 comparing to its surrounding (Rai et al., 2021). This may indicate that this position is natively occupied by water molecules as demonstrated by our native structure.

The heme ligand is well resolved at a resolution of 1.95 Å as revealed by its *2mFo*–*DFc* electron density map (Figure 4B and Figure S2), indicating unambiguous incorporation and binding of the heme in the apo-protein. This is an important finding as crystallization with purified *DdDyP* proteins that have lower *R_Z* values were not successful, which might indicate that the heme on these purified proteins is not well accommodated in the binding pocket, affecting possibly their stability and hence the crystallization (see Table 1). The heme occupies 798 Å² surface area, corresponding to 5.7% of the total surface area of the native structure, similar to that of the cyanide native *DdDyP* structure and other *DdDyP* structures (Rai et al., 2021). PISA analysis indicates that the solvation free energy gain (Δ^iG) of the natively incorporated heme is -22.5 kcal mol⁻¹ with 622 Å² interface area comparing to an average of -22.3 kcal mol⁻¹ for the reconstituted heme of the cyanide native structure (PDB ID: 7O9L) which has an interface interaction area of 609 Å², indicating similar heme binding affinity with slightly better properties for the natively incorporated heme. The van der Waals interactions as well as the hydrogen-bonding network provided by nearby residues and water molecules may contribute to the stabilization of heme binding (Figure 4C) (Sacquin-Mora and Lavery, 2006; Mogharrab et al., 2007). Our analysis shows that the heme is stabilized, along the plane, via its carboxylate oxygens by hydrogen bonding with several water molecules (wat-120, wat-79 and wat-166), and three residues, Glu152, Arg204 and Arg239. The Arg239 interacts weakly with the heme carboxylates oxygens via two hydrogen bonds with a distance of 3.3–3.4 Å, whereas Glu152 and Arg204 form hydrogen bonding with the heme via wat-120 and wat-166, respectively. These interactions indicate that the heme is well stabilized in our model (PDB ID: 8OHY), which confirms the correct geometry of its native incorporation, yielding comparable binding pocket geometry to that prepared with *in vitro* reconstitution (Chen et al., 2015; Rai et al., 2021). Furthermore, the superimposition with the cyanide

native structure indicates a striking similarity (r.m.s.d. = ~ 0.18 Å) around the heme binding pocket including the flanking loop at the proximal side of the heme plane (residues 204-220) (Figure 3D). A side-specific mutagenesis study in DypB found that this proximal loop may have significant role in the heme stability (Rodrigues et al., 2021). This loop has also been implicated in the stabilization of the substrate owing to its flexibility thereby facilitating the substrate/product turnover by flipping in and out around the heme binding site (Liu et al., 2011).

Further, we used the *MOLEonline* tool (<https://mole.upol.cz/online>) to analyse the cavities and tunnels nearby the heme binding pocket and those in long-range distances (Figure S3) (Sehnal et al., 2013). Overall, 14 tunnels were identified, three of which are located next to the heme and perpendicular to each other with characteristics that might have an implication in the *DdDyP* catalysis—entry of substrates and exit of reaction products. These channels may serve as entry gates for H_2O_2 thereby facilitating the enzyme activation required for the oxidative catalysis (Chen et al., 2015; Yoshida et al., 2016; Habib et al., 2019). Two tunnels have average diameter of ~ 3.0 Å, which is sufficient to facilitate the entry of H_2O_2 and perhaps the exit of reaction products of similar size. All tunnels are lined with hydrophobic residues in the middle of the channel as well as several key catalytic residues in the distal and proximal sides of the heme plane. In particular, Arg239, Asp149, His222, Glu152, Ser241, and Thr226 in addition to several hydrophobic residues were found in two proximal channels (Figure S3), which are converged to form a main channel with a length of 42 Å and a diameter of ~ 4.0 Å. The access gate of this channel is lined with charged residues as shown in Figure 4D and E, indicating its implication in the substrate entry. Further, we identified two major cavities at the distal side of the heme plane, of which one cavity (cavity 1) has a volume of 2881 Å³, corresponding to 9.6% of the total surface of *DdDyP* and 4.7 times of the heme molecule. It is located at the heme binding pocket, accommodating the main channel at the binding pocket and extends to the proximal side of the heme plane, indicating a role for this cavity in the catalysis of DyP-peroxidases (Rai et al., 2021; Habib et al., 2019; Yoshida et al., 2011). The second cavity (cavity 2) with approximately half a volume of that of cavity 1 (1411 Å³) is located at the N-terminal region distant from the heme binding pocket and in contact with cavity 2 near the molecular centre of *DdDyP* (Figure S3). The presence of such cavities is important for accommodating wide-range of substrates thereby fulfilling the substrate broad specificity of DyP-type peroxidases (Pfanzagl et al., 2019; Silva et al., 2023).

4 Conclusions

In conclusion, we demonstrated the use of *E. coli* C43(DE3) strain for heterologous expression of *DdDyP* peroxidase, without the use of a heme precursor δ -ALA, hemin chloride or iron supplement, to produce *DdDyP* holoprotein with a natively incorporated heme, relying primarily on the *E. coli* heme biosynthesis by benefiting from the use of enriched medium and low temperature during expression, which yielded an R_z value of ~ 1.0 and a holoprotein with sufficient stability. We further showed, by mean of X-ray crystallography, that the native *DdDyP* expressed in this condition has comparable heme geometry and binding properties. Our study also demonstrates that the natively incorporated heme is well stabilized via hydrogen bonds provided by nearby Arg239, Glu152 and water molecules in addition to van der Waals interactions between the porphyrin rings and surrounding residues within van der Waals distances. Two cavities occupying a total volume of 4292 Å³, corresponding to 14.3% of the total monomeric volume (29951 Å³), were identified. Of which the main cavity (cavity 1) around the heme binding pocket was found to accommodate a large access channel that spans the heme binding pocket. Moreover, the high-quality crystals optimized in this work would be suitable for use as a model for metalloenzymes to study the dynamics and substrate binding kinetics during catalysis. This can be achieved by, for instance, the mixing-and-inject time-resolved serial femtosecond crystallography approach (Pandey et al., 2021), which enables tracking the formation of

the reaction intermediates as well as the mechanism of substrate breakdown into products as demonstrated in other metalloproteins (Worrall and Hough, 2022; Malla and Schmidt, 2022).

5 Conflict of Interest

The authors declare that the research was conducted in the absence of any commercial or financial relationships that could be construed as a potential conflict of interest.

6 Author Contributions

Conceptualization, F.H.M.K.; experiments, Ö.K., L.B., H.H., and F.H.M.K.; formal analysis and data interpretation, F.H.M.K.; Diffraction data collection and processing, F.H.M.K., Ö.K., and S.K.; X-ray structural analysis, F.H.M.K.; contributed funding/reagents/analytic tools, A.P.M; supervised the project, F.H.M.K.; manuscript writing, F.H.M.K. with input from all authors. All authors read and approved the final version of this manuscript.

7 Funding

We acknowledge European XFEL GmbH in Schenefeld, Germany, for provision of biochemistry and x-ray beamtimes at PETRA III/DESY. This work was supported by the European XFEL GmbH internal operational budget for the SPB/SFX instrument.

8 Data availability statement

The crystal structure data was deposited to the protein data bank under the PDB ID: 8OHY and is publicly available under the PDB digital object identifier <http://doi.org/10.2210/pdb8OHY/pdb>.

9 Acknowledgments

We would like to thank the staff members of the SPB/SFX instrument of European XFEL GmbH for fruitful discussion during the conduction of this research. We are grateful to the staff members of the XBI Biolab at European XFEL GmbH for technical support. We acknowledge the use of the XBI Biolab at European XFEL GmbH, enabled by the XBI User Consortium. X-ray diffraction experiments at the P11/PETRA III beamline in DESY were carried out via the proposal no. BAG-20211047 acquired by Huijong Han and Kristina Lorenzen from European XFEL GmbH. We also thank the staff members of the P11/PETRA III beamline at DESY, Hamburg. We thank Richard Bean for the critical reading of the manuscript.

10 References

- Afonine, P.V., Bunkoczi, G., Chen, V.B., Headd, J.J., McCoy, A.J., Moriarty, N.W., Read, R.J., Richardson, D.C., Richardson, J.S., Terwilliger, T.C., and Adams, P.D. (2012). Graphical tools for macromolecular crystallography in PHENIX. *J. Appl. Cryst.* 45, 581–586. doi:10.1107/S0021889812017293
- Burkhardt, A., Pakendorf, T., Reime, B., Meyer, J., Fischer, P., Stübe, N., Penneerselman, S., Lorbeer, O., Stachnik, K., Warmer, M., Rödig, P., Göries, D., and Meents, A. (2016). Status of the

389 crystallography beamlines at PETRA III. *Eur. Phys. J. Plus* 131, 56.
390 <https://doi.org/10.1140/epjp/i2016-16056-0>

391 Bury, C.S., Brooks-Bartlett, J.C., Walsh, S.P., and Garman, E.F. (2018). Estimate your dose:
392 RADDOS-3D. *Protein Sci.* 27, 217–228. doi:10.1002/pro.3302

393 Chen, C., and Li, Tao. (2016). Bacterial dye-decolorizing peroxidases: biochemical properties and
394 biotechnological opportunities. *Phys. Sci. Rev.* 1, 20160051. doi:10.1515/psr-2016-0051
395

396 Chen, C., Shrestha, R., Jia, K., Gao, P.F., Geisbrecht, B.V., Bossmann, S.H., Shi, J., and Li, P. (2015).
397 Characterization of Dye-decolorizing Peroxidase (DyP) from *Thermomonospora curvata*
398 Reveals Unique Catalytic Properties of A-type DyPs. *J. Biol. Chem.* 290, 23447–23463.
399 doi:10.1074/jbc.M115.658807.

400 Collaborative Computational Project, Number 4. (1994). The CCP4 suite: Programs for protein
401 crystallography. *Acta Cryst. D* 50, 760–763. doi:10.1107/S0907444994003112

402 Colpa, D.I., Fraaije, M.W., and van Bloois, E. (2014). DyP-type peroxidases: a promising and versatile
403 class of enzymes. *J. Ind. Microbiol. Biotechnol.* 41, 1–7. Doi:10.1007/s10295-013-1371-6

404 Denninger, J.W., Schelvis, J.P.M., Brandish, P.E., Zhao, Y., Babcock, G.T., and Marletta, M.A. (2000).
405 Interaction of soluble guanylate cyclase with YC-1: kinetic and resonance raman studies.
406 *Biochemistry* 39, 4191–4198. doi:10.1021/bi992332q
407

408 Emsley, P., Lohkamp, B., Scott, W.G., and Cowtan, K. (2010). Features and development of
409 Coot. *Acta Cryst. D* 66, 486–501. doi:10.1107/S0907444910007493
410

411 Fiege, K., Querebillo, C.J., Hildebrandt, P., and Frankenberg-Dinkel, N. (2018). Improved method for
412 the incorporation of heme cofactors into recombinant proteins using *Escherichia coli* Nissle
413 1917. *Biochemistry* 57, 2747–2755. doi:10.1021/acs.biochem.8b00242

414 Francis, D.M., and Page, R. (2010). Strategies to optimize protein expression in *E. coli*. *Curr. Protoc.*
415 *Protein Sci.* 5(1), 5241–52429. doi:10.1002/0471140864.ps0524s61
416

417 Gan, J., Bilal, M., Li, X., Hussain Shah, S.Z., Mohamed, B.A., Hadibarata, T., and Cheng H. (2022).
418 Peroxidases-based enticing biotechnological platforms for biodegradation and
419 biotransformation of emerging contaminants. *Chemosphere.* 307(Pt3), 136035.
420 doi:10.1016/j.chemosphere.2022.136035

421 Habib, M.H., Rozeboom, H.J., Fraaije., and M.W. (2019). Characterization of a new DyP-peroxidase
422 from the alkaliphilic Cellulomonad, *Cellulomonas bogoriensis*. *Molecules* 24, 1208.
423 doi:10.3390/molecules240718

424 Han, H., Round, E., Schubert, R., Gül, Y., Makroczyová, J., Meza, D., Heuser, P., Aepfelbacher, M.,
425 Barák, I., Betzel, C., Fromme, P., Kursula, I., Nissen, P., Tereschenko, E., Schulz, J., Uetrecht,
426 C., Ulicný, J., Wilmanns, M., Hajdu, J., Lamzin, V.S., and Lorenzen, K. (2021). The XBI
427 BioLab for life science experiments at the European XFEL. *J. Appl. Crystallogr.* 54(Pt 1), 7–
428 21. doi:10.1107/S1600576720013989

- 429 Henderson, R. (1990). Cryo-protection of protein crystals against radiation damage in electron and X-
430 ray diffraction. *Proc. R. Soc. B Biol. Sci.* 241, 6–8. doi:10.1098/rspb.1990.0057
- 431 Huang, C.-J., Peng, H.-L., Patel, A.K., Singhanian, R.R., Dong, C.-D., and Cheng, C.-Y. (2021). Effects
432 of Lower Temperature on Expression and Biochemical Characteristics of HCV NS3
433 Antigen Recombinant Protein. *Catalysts* 11, 1297. doi:10.3390/catal11111297
- 434 Kabsch, W. (2010). XDS. *Acta Crystallogr. D. Biol. Crystallogr.* 66(Pt 2), 125–132.
435 doi:10.1107/S0907444909047337
- 436 Kim, S.J., and Shoda, M. (1999). Purification and characterization of a novel peroxidase from
437 *Geotrichum candidum* dec 1 involved in decolorization of dyes. *Appl. Environ. Microbiol.* 65,
438 1029–1035. doi:10.1128/AEM.65.3.1029-1035.1999
- 439 Koua, F.H., Umena, Y., Kawakami, K., and Shen, J.-R. (2013). Structure of Sr-substituted photosystem
440 II at 2.1 Å resolution and its implications in the mechanism of water oxidation. *Proc. Natl.*
441 *Acad. Sci. USA* 110, 3889–3894. doi:10.1073/pnas.1219922110
- 442 Krainer, F.W., Capone, S., Jäger, M., Vogl, T., Gerstmann, M., Glieder, A., Herwig, C., and Spadiut,
443 O. (2015). Optimizing cofactor availability for the production of recombinant heme peroxidase
444 in *Pichia pastoris*. *Microb. Cell Fact.* 14, 4. doi:10.1186/s12934-014-0187-z
- 445 Krissinel, E., and Henrick, K. (2007). Inference of macromolecular assemblies from crystalline state.
446 *J. Mol. Biol.* 372, 774–797. doi:10.1016/j.jmb.2007.05.022
- 447 Layer, G., Reichelt, J., Jahn, D., and Heinz, D.W. (2010) Structure and function of enzymes in heme
448 biosynthesis. *Protein Sci.* 19, 1137–1161. doi:10.1002/pro.405
- 449
- 450 Lemon, C.M., and Marletta, M.A. (2021). Designer heme proteins: achieving novel function with
451 abiological Heme Analogues. *Acc. Chem. Res.* 54, 4565–4575.
452 doi:10.1021/acs.accounts.1c00588
- 453 Liu, X., Du, Q., Wang, Z., Zhu, D., Huang, Y., Li, N., Wie, T., Xu, S., and Gu, L. (2011). Crystal
454 structure and biochemical features of EfeB/YcdB from *Escherichia coli* O157. *J. Biol. Chem.*
455 286, 14922–14931. doi:10.1074/jbc.M110.197780
- 456 Malla, T.N., and Schmidt, M. (2022). Transient state measurements on proteins by time-resolved
457 crystallography. *Curr. Opin. Struct. Biol.* 74, 102376. doi:10.1016/j.sbi.2022.102376
- 458 Owen, R.L., Rudino-Pinera, E., and Garman, E.F. (2006). Experimental determination of the radiation
459 dose limit for cryocooled protein crystals. *Proc. Natl. Acad. Sci. USA* 103, 4912–4917.
460 doi:10.1073/pnas.0600973103
- 461 Pandey, S., Calvey, G., Katz, A. M., Malla, T. N., Koua, F. H. M., Martin-Garcia, J. M., Poudyal, I.,
462 Yang, J.-H., Vakili, M., Yefanov, O., Zielinski, K. A., Bajt, S., Awel, S., Doerner, K., Frank,
463 M., Gelisio, L., Jernigan, R., Kirkwood, H., Kloos, M., Koliyadu, J., Mariani, V., Miller, M.
464 D., Mills, G., Nelson, G., Olmos, J. L., Sadri, A., Sato, T., Tolstikova, A., Xu, W., Ourmazd,
465 A., Spence, J. H. C., Schwander, P., Barty, A., Chapman, H. N., Fromme, P., Mancuso, A. P.,
466 Phillips, G. N., Bean, R., Pollack, L., and Schmidt, M. (2021). Observation of substrate
467 diffusion and ligand binding in enzyme crystals using high-repetition-rate mix-and-inject
468 serial crystallography. *IUCrJ* 8, 878–895. doi:10.1107/S205225251008125

- 469 Park, Y.-J., and Kim, D.-M. (2021). Production of Recombinant Horseradish Peroxidase in an
470 Engineered Cell-free Protein Synthesis System. *Front. Bioeng. Biotechnol.* 9, 778496. doi:
471 10.3389/fbioe.2021.778496
- 472 Pfanzagl, V., Beale, J.H., Michlits, H., Schmidt, D., Gabler, T., Obinger, C., Djinić-Carugo, K., and
473 Hofbauer, S. (2020). X-ray-induced photoreduction of heme metal centers rapidly induces
474 active-site perturbations in a protein-independent manner. *J. Biol. Chem.* 295(39):13488–
475 13501. doi:10.1074/jbc.RA120.014087
- 476 Pfanzagl, V., Bellei, M., Hofbauer, S., Laurent, C.V.F.P., Furtmüller, P.G., Oostenbrink C.,
477 Battistuzzi, G. and Obinger, C. (2019). Redox thermodynamics of B-class dye-decolorizing
478 peroxidases. *J. Inorg. Biochem.* 199, 110761. doi:10.1016/j.jinorgbio.2019.110761
- 479 Rai A., Fedorov R., and Manstein D.J. (2014). Expression, purification and crystallization of a dye-
480 decolorizing peroxidase from *Dictyostelium discoideum*. *Acta Crystallogr. Sect. F Struct.*
481 *Biol. Commun.* 70, 252–255. doi:10.1107/S2053230X14000545
- 482 Rai, A., Klare, J.P., Reinke, P.Y.A., Englmaier, F., Fohrer, J., Fedorov, R., Taft, M.H., Chizhov, I.,
483 Curth, U., Plettenburg, O., and Manstein, D.J. (2021). Structural and Biochemical
484 Characterization of a Dye-Decolorizing Peroxidase from *Dictyostelium discoideum*. *Int. J. Mol.*
485 *Sci.* 22, 6265. doi:10.3390/ijms22126265
- 486 Rodrigues, C.F., Borges, P.T., Scocozza, M.F., Silva, D., Taborda, A., Brissos, V., Frazao, C., and
487 Martins, L.O. (2021). Loops around the heme pocket have a critical role in the function and
488 stability of BsDyP from *Bacillus subtilis*. *Int. J. Mol. Sci.* 22, 10862.
489 doi:10.3390/ijms221910862
- 490 Sacquin-Mora, S., and Lavery, R. (2006). Investigating the local flexibility of functional residues in
491 hemoproteins. *Biophys. J.* 90, 2706–2717. doi:10.1529/biophysj.105.074997
- 492 Salvachúa, D., Prieto, A., Martínez, Á.T., and Martínez, M.J. (2013). Characterization of a novel dye-
493 decolorizing peroxidase (DyP)-type enzyme from *Irpex lacteus* and its application in enzymatic
494 hydrolysis of wheat straw. *Appl. Environ. Microbiol.* 79, 4316–4324.
495 doi:10.1128/AEM.00699-13
- 496 Scocozza, M.F., Martins, L.O., and Murgida, D.H. (2021). Direct electrochemical generation of
497 catalytically competent oxyferryl species of classes I and P dye decolorizing peroxidases. *Int.*
498 *J. Mol. Sci.* 22, 12532. doi:10.3390/ijms222212532
- 499 Sehnal, D., Radka Svobodova, V., Berka, K., Pravda, L., Navratilova, V., Pavel, B., Crina-Maria, I,
500 Michal, O., and Jaroslav, K. (2013). MOLE 2.0: Advanced approach for analysis of
501 biomacromolecular channels. *J. Bioinform.* 5, 39. doi:10.1186/1758-2946-5-39
- 502 Shrestha, R., Chen, X., Ramyar, K.X., Hayati, Z., Carlson, E.A., Bossmann, S.H., Song, L., Geisbrecht,
503 B.V., and Li, P. (2016). Identification of Surface-Exposed Protein Radicals and A Substrate
504 Oxidation Site in A-Class Dye-Decolorizing Peroxidase from *Thermomonospora curvata*. *ACS*
505 *Catal.* 6, 8036–8047. doi:10.1021/acscatal.6b01952
- 506

507 Silva, D., Rodrigues, C.F., Lorena, C., Borges, P.T., and Martins, L.O. (2023). Biocatalysis for
508 biorefineries: The case of dye-decolorizing peroxidases. *Biotechnol. Adv.* 65, 108153.
509 doi:10.1016/j.biotechadv.2023

510 Singh, R., Grigg, J.C., Armstrong, Z., Murphy, M.E., and Eltis, L.D. (2012). Distal heme pocket
511 residues of B-type dye-decolorizing peroxidase: arginine but not aspartate is essential for
512 peroxidase activity. *J. Biol. Chem.* 287, 10623–10630. doi:10.1074/jbc.M111.332171

513 Strittmatter, E., Wachter, S., Liers, C., Ullrich, R., Hofrichter, M., Plattner, D.A., and Piontek, K.
514 (2013). Radical formation on a conserved tyrosine residue is crucial for DyP activity. *Arch.*
515 *Biochem. Biophys.* 537, 161–167. doi:10.1016/j.abb.2013.07.007

516 Sugano, Y., and Yoshida, T. (2021). DyP-type peroxidases: recent advances and perspectives. *Int. J.*
517 *Mol. Sci.* 22, 5556–5570. doi:10.3390/ijms22115556

518 Sugano, Y., Sasaki, K., and Shoda, M. (1999). cDNA cloning and genetic analysis of a novel
519 decolorizing enzyme, peroxidase gene dyp from *Geotrichum candidum* Dec 1. *J. Biosci.*
520 *Bioeng.* 87, 411–417. doi:10.1016/s1389-1723(99)80087-5

521 Umena, Y., Kawakami, K., Shen, J.-R., and Kamiya, N. (2011). Crystal structure of oxygen-evolving
522 photosystem II at a resolution of 1.9 Å. *Nature* 473, 55–60. doi:10.1038/nature09913

523 Vogel, K.M., Hu, Z., Spiro, T.G., Dierks, E.A., Yu, A.E. and Burstyn, J.N. (1999). Variable Forms of
524 Soluble Guanylyl Cyclase: Protein-Ligand Interactions and the Issue of Activation by Carbon
525 Monoxide. *J. Biol. Inorg. Chem.* 4, 804–813. doi:10.1007/s007750050354

526 Worrall, J.A.R., and Hough, M.A. (2022). Serial femtosecond crystallography approaches to
527 understanding catalysis in iron enzymes. *Curr. Opin. Struct. Biol.* 77, 102486.
528 doi:10.1016/j.sbi.2022.10.2486

529 Yoshida T., Ogola H., Amano Y., Hisabori T., Ashida H., Sawa Y., Tsuge H., and Sugano Y. (2016).
530 *Anabaena* sp. DyP-type peroxidase is a tetramer consisting of two asymmetric dimers. *Proteins*
531 84, 31–42. doi:10.1002/prot.24952.

532 Yoshida, T., and Sugano, Y. (2023). Unexpected diversity of dye-decolorizing peroxidases. *Biochem.*
533 *Biophys. Rep.* 33, 101401. doi:10.1016/j.bbrep.2022.101401.

534 Yoshida, T., Tsuge, H., Konno, H., Hisabori, T., and Sugano, Y. (2011). The catalytic mechanism of
535 dye-decolorizing peroxidase DyP may require the swinging movement of an aspartic acid
536 residue. *FEBS J.* 278, 2387–2394. doi:10.1111/j.1742-4658.2011.08161.x

537 Zubieta, C., Krishna, S.S., Kapoor, M., Kozbial, P., McMullan, D., Axelrod, H.L., Miller, M.D.,
538 Abdubek, P., Ambing, E., Astakhova, T., Carlton, D., Chiu, H.J., Clayton, T., Deller, M.C.,
539 Duan, L., Elsliger, M.A., Feuerhelm, J., Grzechnik, S.K., Hale, J., Hampton, E., Han, G.W.,
540 Jaroszewski, L., Jin, K.K., Klock, H.E., Knuth, M.W., Kumar, A., Marciano, D., Morse, A.T.,
541 Nigoghossian, E., Okach, L., Oommachen, S., Reyes, R., Rife, C.L., Schimmel, P., van den
542 Bedem, H., Weekes, D., White, A., Xu, Q., Hodgson, K.O., Wooley, J., Deacon, A.M.,
543 Godzik, A., Lesley, S.A., and Wilson, I.A. (2007). Crystal structures of two novel dye-
544 decolorizing peroxidases reveal a beta-barrel fold with a conserved heme-binding motif.
545 *Proteins* 69, 223–33. doi:10.1002/prot.21550

546

TABLES

Table 1 Characterization of the native heme incorporation into *DdDyP* expressed in *E. coli* C43(DE3) at different conditions, the protein yield and crystallization trials

Overexpression	Soret peak (nm)	R_Z value (A_{soret}/A_{280})	Heme content (%) [†]	Protein yield (mg) [‡]	Crystallization hits
LB at 37 °C	406	0.27	26.5	1.2	No
LB at 20 °C	405	0.502	49.3	2.96	No
2×YT at 20 °C	402	0.93	90	14.1	Yes
Reference*	406	1.02	100	1.2	Not tested

*The reference is the *DdDyP* with a reconstituted heme; from LB expression. [†]Heme content relevant to the reference value in this study, which was set to 100%. [‡]The yield is normalized to 25.0 g of wet weight of overexpressed cells used for purification.

568 **Table 2** X-ray diffraction data collection and crystallography refinement statistics

	Native <i>DdDyP</i> structure
PDB ID	8OHY
Data Collection	
Beamline	P11/PETRA III at DESY
Photon Energy (keV)	12.0
Photon flux (ph . s ⁻¹)	~2 × 10 ¹⁰
Radiation dose (MGy)	~0.58
Space group	<i>P</i> 4 ₁ 2 ₁ 2
Cell dimensions	
a, b, c (Å)	99.88 99.88 73.12
α, β, γ (°)	90.00 90.00 90.00
Resolution (Å)	44.67–1.95 (2.02–1.95)*
<i>R</i> _{merge} [†]	0.2715 (4.643)*
<i>I</i> /σ <i>I</i>	12.02 (0.6)*
Completeness (%)	98.54 (91.55)*
Multiplicity	26.7 (26.0)*
<i>CC</i> _{1/2}	0.999 (0.411)*
<i>CC</i> *	1.0 (0.764)*
Wilson <i>B</i> -factor (Å ²)	36.8
Refinement	
Resolution range (Å)	44.67–1.95
No. of reflections (unique)	27129 (2471)*
<i>R</i> _{work} / <i>R</i> _{free} [‡]	0.206 (0.400)* / 0.247 (0.445)*
No. of atoms	2662
Protein	2459
Ligands	74
Solvent	163
No. of residues	306
Average <i>B</i> -factor (Å ²)	41.29
Protein	41.23
Ligands	39.63
Solvents	42.76
r.m.s. deviations	
Bonds (Å)	0.005
Angles (°)	0.71
Ramachandran (%)	
Favored	98.03
Allowed	1.97
Outliers	0.00
Rotamer outliers (%)	0.00
Clashscore	1.00

569 *Values in parenthesis are of the highest resolution shell. [†]*R*_{merge} = $\sum_h \sum_i |I_i(h) - \langle I(h) \rangle| /$
570 $\sum_h \sum_i |I_i(h)|$, where *I_i(h)* is the intensity measurement for a reflection *h* and $\langle I(h) \rangle$ is the mean
571 intensity for this reflection. [‡]*R*_{work} = $\sum_h ||F_{obs}| - |F_{calc}|| / \sum_h |F_{obs}|$ and *R*_{free} was calculated
572 using a randomly (5.0%) selected reflections.

SCHEME AND FIGURE LEGENDS

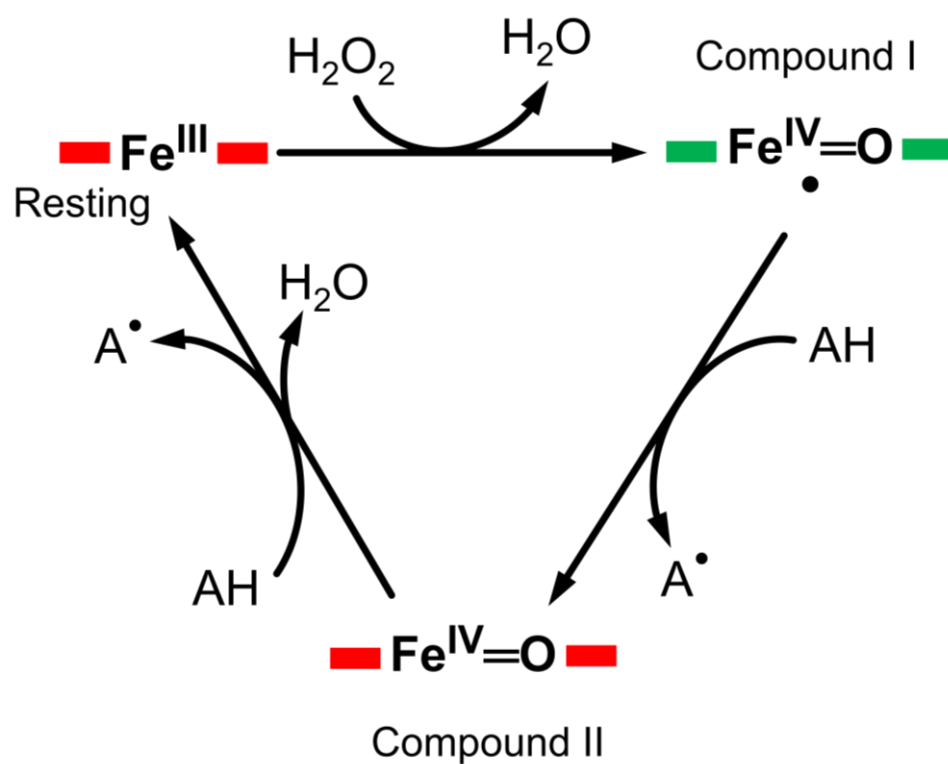
Scheme 1 A typical enzymatic cycle of DyP-type peroxidases showing the interconversion between the resting state (ferric porphyrin), compound I heme oxoferryl species (porphyrin cationic radical) $[\text{Fe(IV)=O Por}^\bullet]^+$; and compound II intermediate state, $[\text{Fe(IV)=O}]^+$. The AH is the reducing substrate which is oxidized into an intermediate radical product (A^\bullet) during catalysis.

Figure 1 Purification, characterization and crystallization of *DdDyP*. (A) An SDS-PAGE showing the glutathione sepharose affinity purification. Lane M, protein marker; FT lane, flow-through of the unbound proteins from the lysate; W-1 lane, step 1 washing of the Glutathione Sepharose column; and W-2, the second washing step of the column after elution (B) the HRV 3C digestion of GST-*DdDyP* expressed protein complex and GST-free *DdDyP* protein. (C) The Gel-filtration profile of purified *DdDyPs* and representative samples from 2×YT expressed at 37 and 20 °C, and LB at 37 °C, and (D) brownish crystals from two different purification batches of independently overexpressed *DdDyP* protein. The scale bar in “D” represents 100 μm.

Figure 2 UV-visible electronic absorbance of *DdDyP* of different overexpression conditions. (A) a typical spectrum of a purified *DdDyP* when expressed in LB medium at 37 °C, (B) and (C) *DdDyP* electronic spectra when expressed at 20 °C in LB and 2×YT medium, respectively. The ET *Q*-band and charge transfer band in the region from 500–700 nm of the 2×YT condition are described in (C). (D) The reference UV-visible spectra of LB *DdDyP* after reconstitution with hemin chloride, and the small box in (D) represents a magnified view of the *Q*-band and charge transfer regions from 500–685 nm.

Figure 3 Overall structure of native *DdDyP* and its superposition with native cyanide *DdDyP* structure (PDB code: 7O9L). (A) Topology representation of the *DdDyP*-type peroxidase. (B) Overall structure of monomeric *DdDyP* showing the ferredoxin-like folds at the N- and C-terminals colored according to (A). (C) Superimposition of native *DdDyP* structure (green) into a cyanide native structure (gray). (D) Electrostatic potentials surface of native *DdDyP* colored from -5.7 kT (red) to +5.7 kT (blue) calculated using the program PyMOL (<http://www.pymol.org/pymol>). The yellow dashed circle highlights the heme binding pocket and possible pathway for H_2O_2 and/or substrate entry.

Figure 4 Monomeric structure of the native *DdDyP* highlighting the heme binding pocket at a resolution of 1.95 Å (PDB code: 8OHY) and the channel characteristics of the system. (A) The overall monomeric structure of *DdDyP* highlighting its heme binding pocket (black box). (B) The $2m\text{Fo}-D\text{Fc}$ electron density map (gray mesh) contoured at 1.0 sigma level displaying a magnified view of the heme binding pocket (active site). (C) The hydrogen bonding network (black dots) of the heme binding pocket at the distal and proximal sites of the heme plane. The two water molecules (wat-182 and wat-184) liganded to the heme-Fe(III) via hydrogen bond are highlighted in black, while the conserved key residues are displayed as yellow stick. All figures were generated using PyMOL software (<http://www.pymol.org/pymol>). (D) Two-dimensional representation of a large pore spanning the C-terminal region across the distal site of the heme binding pocket as a result of two channel convergence colored according to the hydropathy scores of the lining residues. (E) A 3D representation of the channel shown on (D).



Scheme 1 Kalkan et al

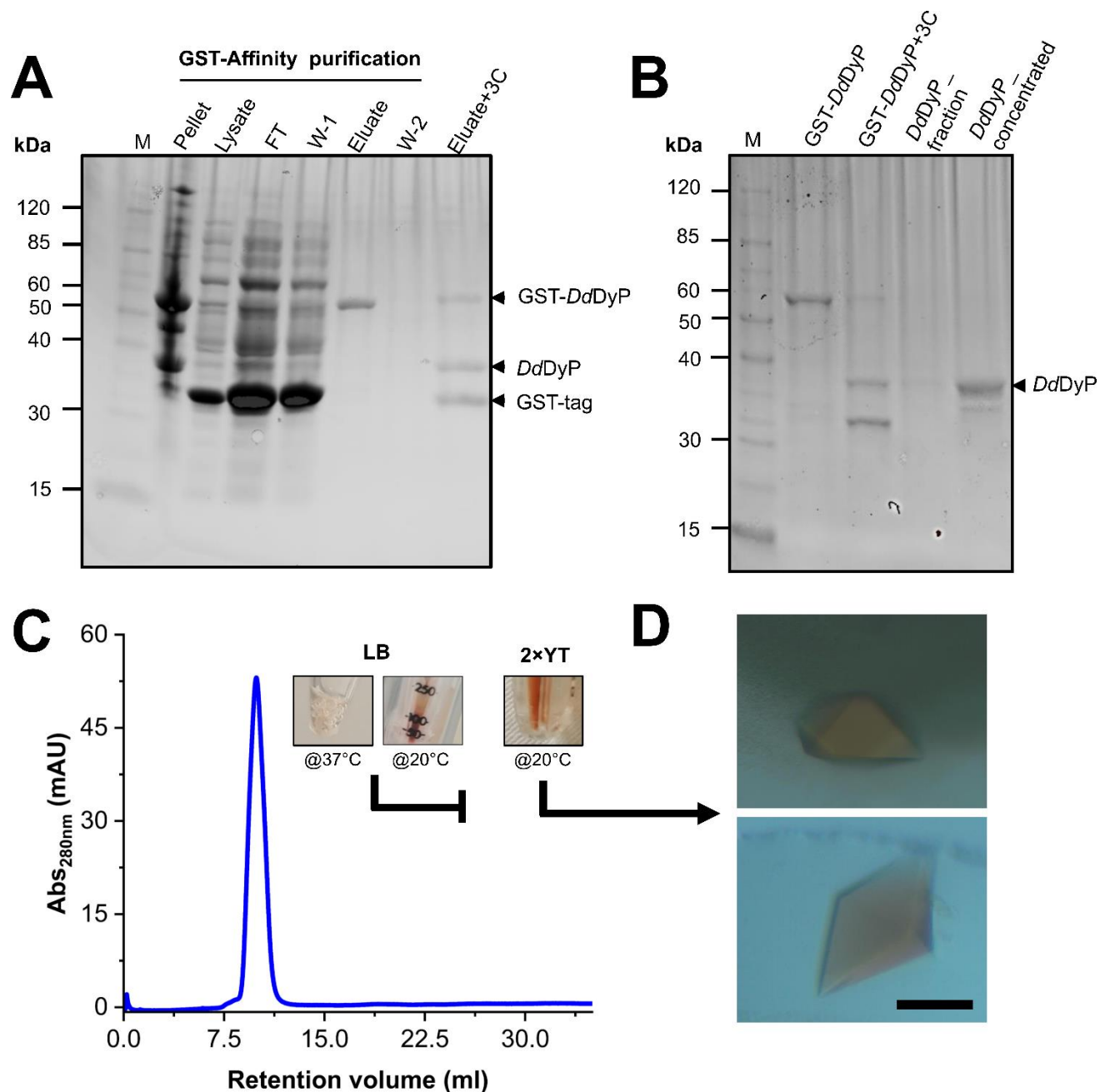


Figure 1 Kalkan et al

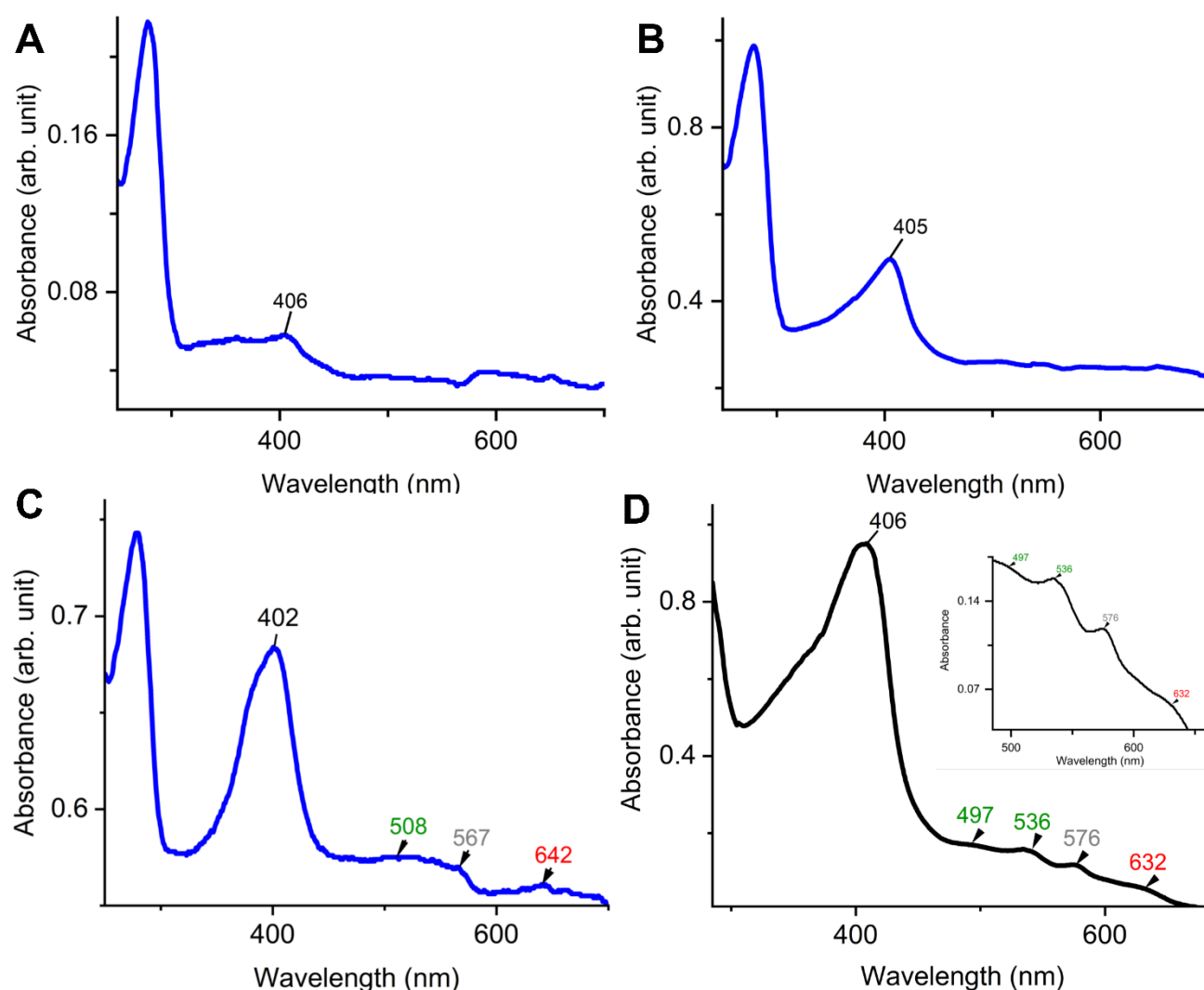


Figure 2 Kalkan et al

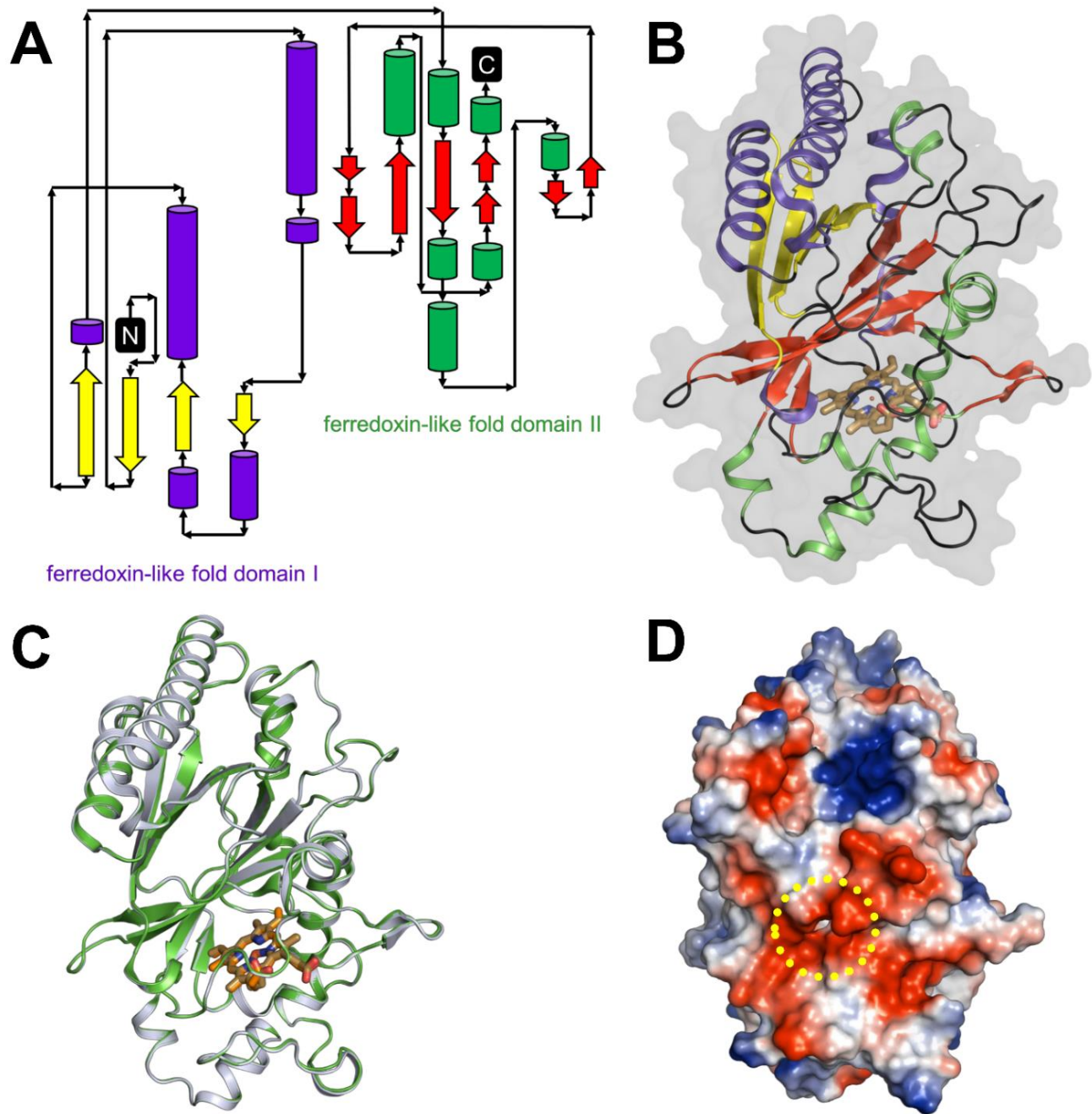


Figure 3 Kalkan et al

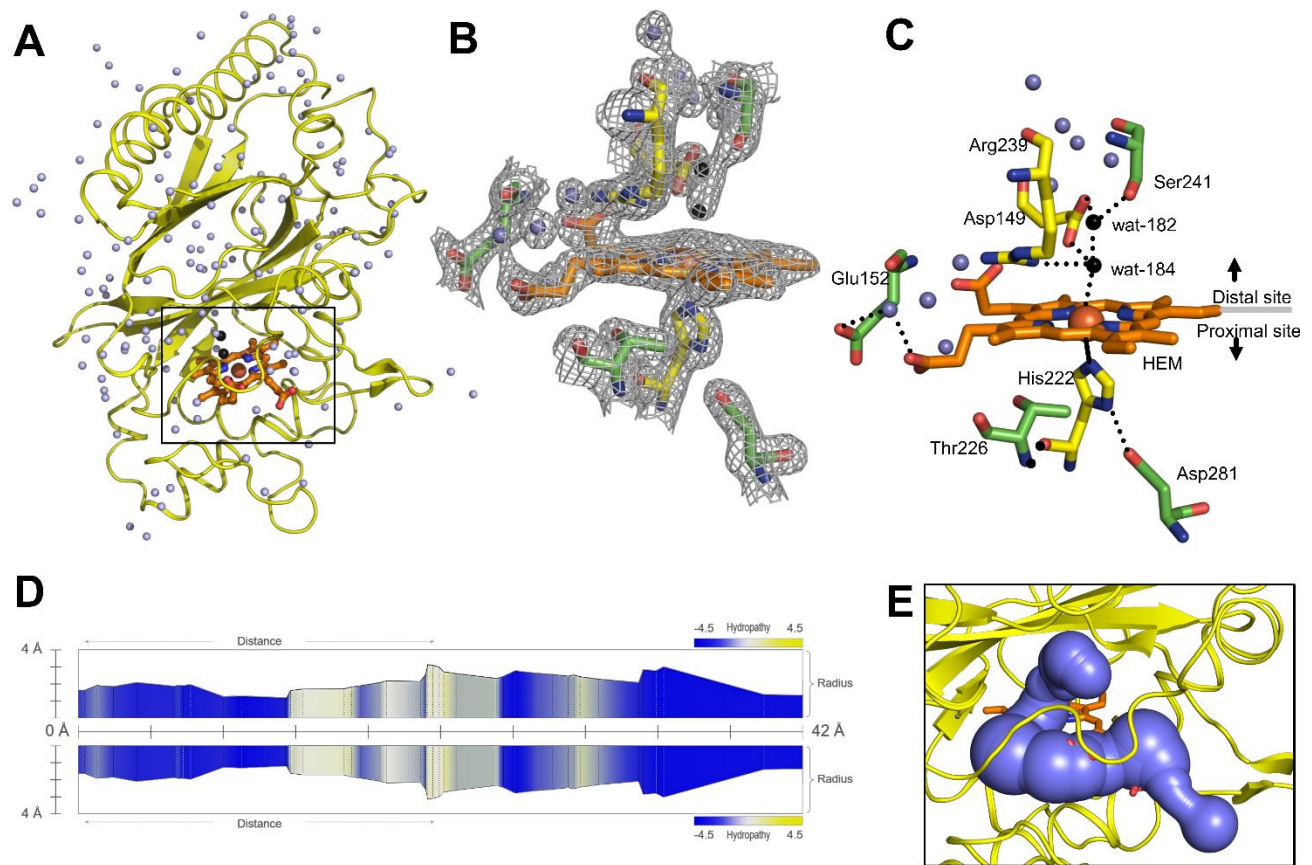


Figure 4 Kalkan et al